Effects of Ta^{5+} Substitution on the Structure and Photocatalytic Behavior of the $Ca_2Nb_2O_7$ Photocatalyst

Liwu Zhang,[†] Hongbo Fu,[‡] Chuan Zhang,[†] and Yongfa Zhu*,[†]

Department of Chemistry, Tsinghua University, Beijing, 100084, People's Republic of China, and Department of Environmental Science and Engineering, Fudan University, Shanghai, 200433, People's Republic of China

Received: May 27, 2007; In Final Form: November 24, 2007

Nanosized $Ca_2Nb_{2-x}Ta_xO_7$ ($0 \le x \le 2$) photocatalysts were synthesized at 160 °C by hydrothermal methods. The absorption onset of $Ca_2Nb_{2-x}Ta_xO_7$ ($0 \le x \le 2$) photocatalysts shifted to shorter wavelengths with an increase of tantalum molar ratio. On the basis of theoretical calculations, the conduction band level of $Ca_2Nb_{2-x}Ta_xO_7$ became higher, and the curvature of the conduction band became larger with an increase of tantalum content due to the different electronegativities of Ta 5d and Nb 4d. The photocatalytic activity of $Ca_2Nb_2O_7$ slightly decreased with a small molar ratio of tantalum substitution ($x \le 0.8$), while the activity can be effectively improved with a large molar ratio of tantalum substitution ($x > 0.8$). The increase of activity as $x > 0.8$ can be attributed to more effective photoelectron transfer in the conduction band with larger curvature, and the slight decrease of activity as $x \le 0.8$ is attributed to the decreased amount of absorbed photons and lattice distortion, which can act as recombination centers.

1. Introduction

Mixed metal oxides with the $A_2M_2O_7$ pyrochlore structure are of considerable interest as catalysts and electrocatalysts for hydrocarbon oxidation reactions, in thick film resistor applications, and for their properties as ionic conductors.[1] In recent years, it has been found that $A_2M_2O_7$ with a pyrochlore structure also showed photocatalytic activity.[2,3]

Recent studies have shown that the substitution of the M site with other metal ions could considerably improve the catalytic activity.[4−6] The substitution of the M sites might induce a slight modification of the crystal structure due to the different ion radii, resulting in a dramatic influence on the mobility of the charge carrier and a change in the photocatalytic and photophysical properties.[7] However, as most reports of substitution effects were focused on the photocatalytic activity of water splitting,[4−7] few reports exist concerning the field of the photooxidation of organic compounds.[8] Theoretical studies using density functional theory (DFT) calculations for the purpose of probing the correlation between band structure and photocatalytic activity in substituted photocatalysts is still reported poorly.

On the other hand, the preparation of nanoscale mixed oxides (such as $A_2Nb_{2-x}Ta_xO_7$) is still a challenge. $A_2Nb_{2-x}Ta_xO_7$ can be obtained thus far in a pure form only by a conventional solid-state reaction (SSR) route or sol−gel method.[4,6] It is difficult for the SSR route to control crystallinity and particle size, localized segregation of components, and stoichiometry due to high temperatures. For several applications, particularly as catalysts and for screen printing resistors, synthesis at low temperatures is desirable to produce powders with a small particle size and high surface area. Many low-temperature methods such as sol−gel or precipitation routes require a calcination tip in the process for the formation of the final product, which results in some loss of surface area. Direct low-temperature hydrothermal crystallization of mixed metal oxides avoids this calcination step and is particularly advantageous for the preparation of high surface area catalytic materials.

Here, we attempted to prepare $Ca_2Nb_2O_7$ photocatalysts with Ta substitution of the Nb sites. $Ca_2Nb_2O_7$ and $Ca_2Ta_2O_7$ both have good dielectric properties.[9] The $Ca_2Nb_2O_7$−$Ca_2Ta_2O_7$ system in the vicinity of ambient temperature with low temperature coefficient of the dielectric constant (TCK) and dielectric loss shows that it is expected to be competitive with materials presently in use in this rapidly expanding technology and may prove to be advantageous with further development.[10] The synthesis of pyrochlore $Ca_2Nb_2O_7$ and $Ca_2Ta_2O_7$ has been widely reported. With the SSR method, a high temperature of 1365 °C was required for phase-pure $Ca_2Ta_2O_7$ pyrochlore,[11] but high-temperature synthesis of $Ca_2Nb_2O_7$ resulted in the formation of a phase with a perovskite structure.[12] Lamure and Colas[13] attempted the preparation of $Ca_2Nb_2O_7$ pyrochlore by the reaction of CaF_2 with Nb_2O_5 at 1100 °C and CaO with NbO_2 at 1350 °C, and single phase products were not observed. Lewandowski and Pickering once used ethoxide as the resource and successfully synthesized $Ca_2Nb_2O_7$ and $Ca_2Ta_2O_7$ under hydrothermal conditions,[14] but the synthesis process was too complex and expensive. In this work, we used Nb_2O_5 and Ta_2O_5 acting with excess $Ca(OH)_2$ through a simple hydrothermal process and successfully synthesized $Ca_2Nb_2O_7$ photocatalysts with different molar ratios of Ta substitution, and the photocatalytic oxidation activity was evaluated by the decomposition of gaseous formaldehyde (FAD) and rhodamine B (RhB). Theoretical calculations were performed to investigate the effect of Ta substitution on the electronic structure of $Ca_2Nb_2O_7$, and the photophysical properties, photocatalytic properties, and substitution effect were systematically investigated.

2. Experimental Procedures

2.1. Synthesis of the Photocatalyst. Powders of $Ca_2Nb_{2-x}Ta_xO_7$ with $x = 0$, 0.4, 0.8, 1.0, 1.2, 1.6, and 2.0 were prepared by the hydrothermal method. In a typical synthesis procedure,

* To whom correspondence should be addressed. Tel.: +86-10-62783586; fax: +86-10-62787601; e-mail: zhuyf@tsinghua.edu.cn.
[†] Tsinghua University.
[‡] Fudan University.

10.1021/jp074092r CCC: $40.75
Published on Web 02/01/2008

2.5 mmol of Nb_2O_5, Ta_2O_5 with a required stoichiometry, and 50 mmol of $Ca(OH)_2$, respectively, were added to a Teflon-lined autoclave with the capacity of 50 mL. Then, 30 mL of distilled water was added, and the autoclave was sealed after simple stirring. The autoclave was maintained at 160 °C for 24 h without further stirring and then cooled to room temperature naturally. The excess $Ca(OH)_2$ was used up by adding a HCl solution to pH 1. Finally, the deposit was quickly filtered off, washed with distilled water several times, and dried in air at 80 °C.

2.2. Analysis Techniques. X-ray diffraction (XRD) experiments were carried out using a Rigaku DMAX-2400 diffractometer with Cu Kα radiation. The average crystal size was determined from XRD pattern parameters according to the Scherrer equation: $D_c = K\lambda/\beta \cos\theta$. D_c is the average crystal size, K is the Scherrer constant equal to 0.89, β is the full width at half-maximum (fwhm), and θ is the diffraction angle. The peak at 14.9° was used for the calculation of the crystal size because it had a relatively strong intensity and did not overlap with the other diffraction peaks. The grain size was measured using a Hitachi H-800 transmission electron microscope. The accelerating voltage of the electron beam was 200 kV. Raman spectra were acquired with a Raman spectrometer (Renishaw 1000 NR) using an Ar ion laser (632.8 nm). Raman spectra were measured under a microscope using a 20 objective lens to focus the incident excitation laser radiation into a spot 1−2 or 2−3 μm in diameter and to collect the scattered light. The laser power was kept low enough to avoid heating the samples by optical filtering and/or defocusing the laser beam at the sample surface. Spectra were collected in the range of 1000−200 cm^{-1} with a resolution of 1 cm^{-1}. UV−vis diffuse reflectance spectrums (DRS) of the samples were measured using a Hitachi U-3010 UV−vis spectrophotometer.

2.3. Photocatalytic Reactions. The photocatalytic activities of the as-prepared samples were first evaluated by the decomposition of FAD. An 11 W UV light lamp ($\lambda = 254$ nm, the Institute of Electric Light Sources) was used. The photoreactor used was a 400 mL cylindrical quartz vessel, which consisted of an inlet, an outlet, and a sample port. A total of 0.1 g of as-prepared $Ca_2Nb_{2-x}Ta_xO_7$ was dispersed in about 1 mL of ethanol. The solution was dripped onto a clean glass slide and was made to spread on the slide uniformly. When the solution evaporated, a coated slide was generated. The blank glass slide or coated slide was tested in the vessel perpendicular to the light beam. The area of the glass slide was 7.5 cm × 2.5 cm. The distance between the film and the light source was 5 cm, where the light intensity was measured to be 120 $\mu W/cm^2$. A mixture that contained FAD of about 1800 ppm was then forced into the photoreactor. Then, the photoreactor was sealed, and the photocatalytic reaction was started by turning on the UV lamp. The concentration of FAD was measured by a SP-502 gas chromatograph equipped with a flame ionization detector (FID) and a 2 m stainless steel column (GDX-403) at 373 K.

The photocatalytic activities were further evaluated by the decomposition of rhodamine B (RhB) during irradiation with UV ($\lambda = 254$ nm). The UV light was obtained by a 12 W Hg lamp (Institute of Electric Light Sources), and the average light intensity was 150 $\mu W\ cm^{-2}$. The irradiation area was approximately 40 cm^2. The radiant flux was measured with a power meter from the Institute of Electric Light Sources. Aqueous suspensions of RhB (usually 100 mL, 1×10^{-5} M) and 50 mg of the powder were placed in a vessel. Prior to irradiation, the suspensions were magnetically stirred in the dark for ca. 30 min to ensure the equilibrium of the working solution.

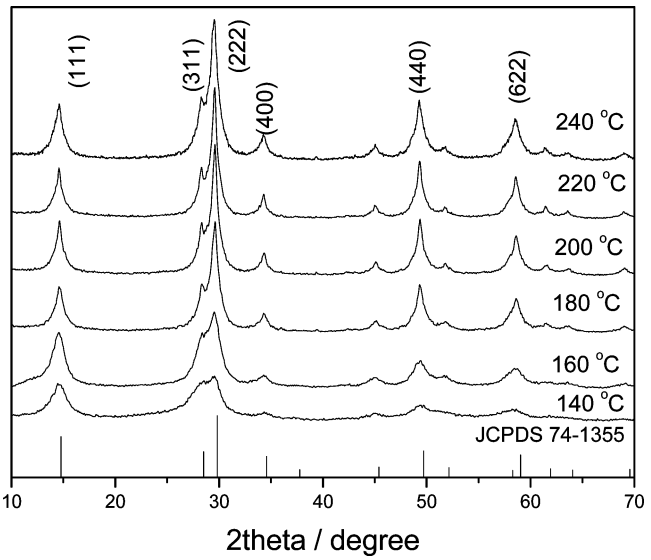

Figure 1. XRD patterns of $Ca_2Ta_2O_7$ prepared under different hydrothermal temperatures for 24 h.

The suspensions were kept under constant air-equilibrated conditions before and during irradiation. The pH value of the reaction suspension was not adjusted. At given time intervals, 3 mL aliquots were sampled and centrifuged to remove the particles. The filtrates were analyzed by recording the variations of the absorption band maximum (553 nm) in the UV−vis spectra of the dyes using a Hitachi U-3010 spectrometer.

Photoelectrochemical measurements were carried out in a 100 mL glass reactor under UV illumination. An 11 W bacterial lamp was used as the UV light source. For photocurrent measurements, 25 mg of photocatalyst was suspended in distilled water (75 mL) containing acetate (1 M) and Fe^{3+} (1 mM) as an electron donor and acceptor, respectively. The pH value of the suspension was adjusted to 1.95 ± 0.05 with $HClO_4$. A platinum plate (1 cm × 1 cm, 0.125 mm thick, both sides exposed to the solution), a saturated calomel electrode (SCE), and platinum gauze were immersed in the reactor as a working (collector), reference, and counter electrode, respectively. Photocurrents in the suspension were measured by applying a potential (+0.6 V vs SCE) to the Pt working electrode using a potentiostat (CHI-660B).

3. Results and Discussion

3.1. Effect of Ta^{5+} Substitution on the Structure of $Ca_2Nb_2O_7$. To determine the optimum hydrothermal temperature for Ta^{5+} substitution, $Ca_2Ta_2O_7$ was first prepared under different hydrothermal temperatures between 140 and 240 °C. XRD patterns are shown in Figure 1. All the reflections of the sample can be exactly indexed as the pure cubic $Ca_2Ta_2O_7$ pyrochlore structure (JCPDS 74−-1355). The crystallization of pyrochlore-type $Ca_2Ta_2O_7$ occurred during the hydrothermal treatment at 140 °C, and a better $Ca_2Ta_2O_7$ single pyrochlore phase was obtained above 160 °C. With the increase of hydrothermal temperature, the diffraction peaks were intensified and became sharper, indicating a favorability of high temperature for the formation of $Ca_2Ta_2O_7$ crystals. The average crystal size of as-prepared $Ca_2Ta_2O_7$ was estimated according to the Scherrer equation. The peak at 14.8° was used for the crystal size calculation. The average crystal size of the as-prepared samples was only about 5 nm. We thus decided on the preparation temperature for $Ca_2Nb_{2-x}Ta_xO_7$ at 160 °C as will be discussed later.

Figure 2 shows XRD patterns of $Ca_2Nb_{2-x}Ta_xO_7$ ($x = 0-2$) samples prepared by the hydrothermal method at 160 °C for

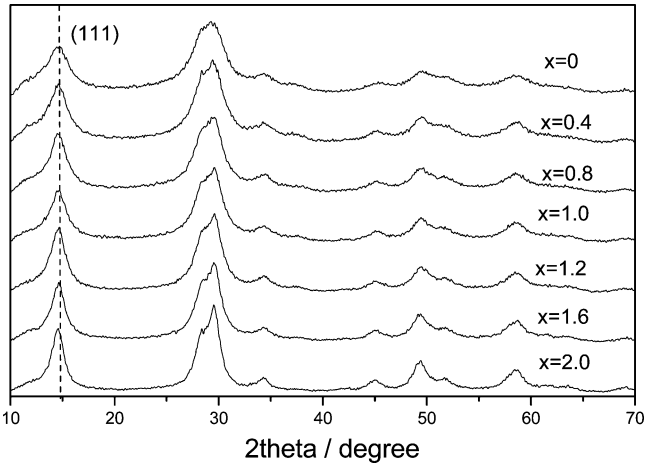

Figure 2. XRD patterns of $Ca_2Nb_{2-x}Ta_xO_7$ ($x = 0-2$) prepared at 160 °C for 24 h.

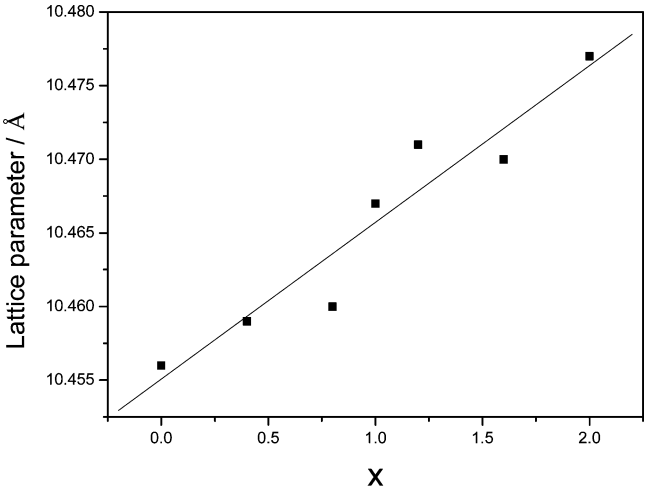

Figure 3. Evolution of the lattice parameters with the composition.

24 h. It is important to note that no reflections from Nb_2O_5, Ta_2O_5, or other species were observed as distinct impurities, implying an improved mixing of the constituent cations in the as-prepared samples. The similarity of the diffractograms suggests that these compounds are isostructural with pyrochlore $Ca_2Nb_2O_7$, with only slight shifts in 2θ values being observed for several diffraction peaks. The evolution of the lattice parameters with the composition is shown in Figure 3. The cubic cell constant of a values was calculated using the 111 ($2\theta \approx 15°$) line and considering the cubic symmetry reported in the JCPDS card file of $Ca_2Nb_2O_7$. When the content of Ta increases, it can be observed that a increases regularly. A similar trend of the lattice parameter evolution was previously evidenced[15,16] but cannot be rationalized on the basis of the respective ionic radii of Nb^{5+} and Ta^{5+}, which are identical (0.74 Å),[17] as a consequence of the so-called lanthanide contraction. In the present work, the $Ca_2Nb_{2-x}Ta_xO_7$ solid solution was prepared under low temperature via a hydrothermal process, and the resulting solid solution has many defects. Therefore, the lattice parameter variation is not as uniform as that in the case of the solid solution prepared by the solid-state reaction method. However, these observations strengthen the idea that the direct substitution of Ta^{5+} for the Nb site in $Ca_2Nb_2O_7$ is possible, and the ternary compounds were synthesized as single $Ca_2Nb_{2-x}Ta_xO_7$ phases corresponding to a continuous series of solid solutions between $Ca_2Nb_2O_7$ and $Ca_2Ta_2O_7$. The XRD pattern of $Ca_2Nb_2O_7$ had considerably broader peaks than that

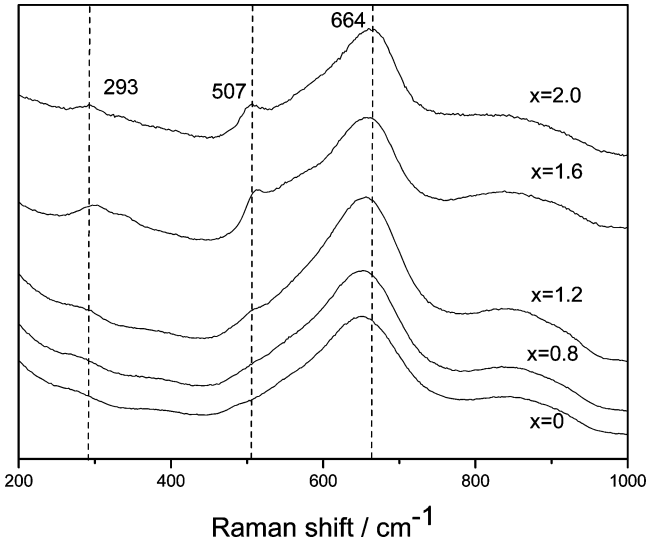

Figure 4. Raman spectra of $Ca_2Nb_{2-x}Ta_xO_7$ ($x = 0-2$) samples.

of $Ca_2Ta_2O_7$, and the diffraction peaks became sharper as the Ta content increased, revealing that the crystal sizes of the solid solutions grew gradually larger with increasing Ta content.

Raman spectra of the $Ca_2Nb_{2-x}Ta_xO_7$ samples are shown in Figure 4. The peaks around 297, 503, and 664 cm^{-1} were observed for all samples. The bands at 293 cm^{-1} arose from the breathing vibration of the long M−O (M═Nb or Ta) bonds and M−O−M (bridging O atom) T_{2g} bending mode.[18] The peak at 507 cm^{-1} resulted from A_{1g} (Ta/Nb) modes. In the case of Ta_2O_5, the major band at 621 cm^{-1} is the characteristic band that comes from the TaO_6 octahedra-sharing corner structure.[19] In the case of tantalates, the band at 621 cm^{-1} was shifted to 664 cm^{-1}, indicating that the formation of $Ca_2Ta_2O_7$ ruptures the corner-sharing structure of Ta−O polyhedra in Ta_2O_5. The main band in the Raman spectra of $Ca_2Nb_{2-x}Ta_xO_7$ at 600−750 cm^{-1} is attributed to the M−O stretching mode of the M−O−M chains, which is mainly due to a totally symmetric combination of coupled M−O stretching modes in the chains of tantalum or niobium octahedra. When the Ta content increases, the main band at 600−750 cm^{-1} is shifted to higher wavenumbers, which could be attributed to the different metal−oxygen bond lengths in TaO_6 and NbO_6 octahedra.

Figure 5 shows TEM images of the as-prepared nanosized $Ca_2Nb_2O_7$ and $Ca_2Ta_2O_7$ samples. On the basis of TEM observations in Figure 5, the particle size of $Ca_2Nb_2O_7$ and $Ca_2Ta_2O_7$ was very small. The particle size was nearly uniformly dispersed and only about 4−5 nm on average, which is consistent with XRD results. The ultra-fine nanoparticles congregated due to their high surface energy.

3.2. Effect of Ta^{5+} Substitution on Photoabsorption Properties of $Ca_2Nb_2O_7$. UV−vis diffuse reflectance spectra of $Ca_2Nb_{2-x}Ta_xO_7$ photocatalysts prepared by the hydrothermal method are shown in Figure 6. With an increasing amount of Ta substitution, the absorbance onset of the sample showed a shift to shorter wavelengths. For a crystalline semiconductor, it was shown that the optical absorption near the band edge follows the equation[33,34]

$$\alpha = A(h\nu - E_g)^{n/2}/h\nu$$

where α, ν, E_g, A, and n are the absorption coefficient, incident light frequency, band gap, constant, and an integer, respectively. The integer n depends on the characteristics of the optical transition ($n = 1$, 2, 4, and 6). The value of n as determined for

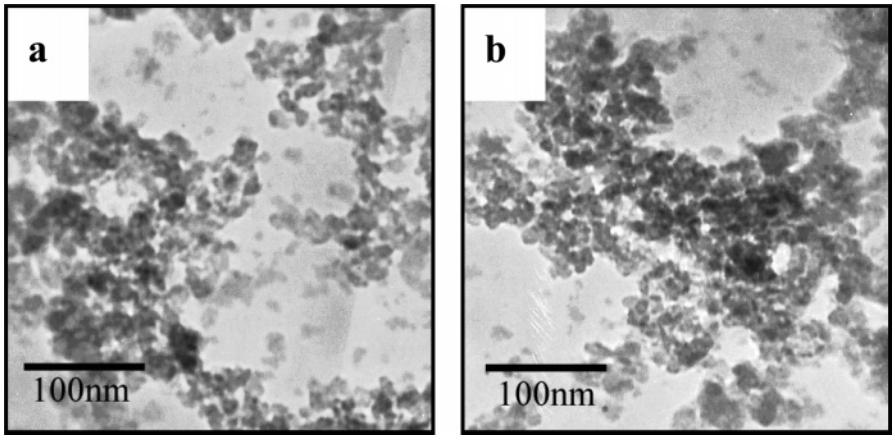

Figure 5. TEM images of as-prepared ultrafine $Ca_2Nb_2O_7$ and $Ca_2Ta_2O_7$ nanoparticles. (a) $Ca_2Nb_2O_7$ and (b) $Ca_2Ta_2O_7$.

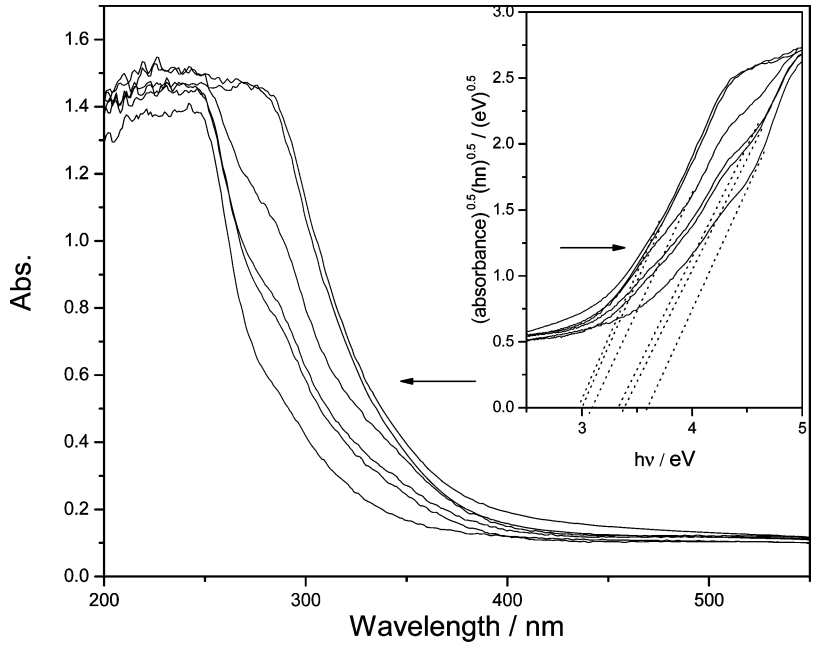

Figure 6. UV−vis diffuse reflectance spectra of $Ca_2Nb_{2-x}Ta_xO_7$ photocatalysts. Arrow direction: $x = 0$, 0.4, 0.8, 1.2, 1.6, 2.0.

$Ca_2Nb_{2-x}Ta_xO_7$ is 1, indicating that a direct optical transition can occur with no significant change in the wave vector for $Ca_2Nb_{2-x}Ta_xO_7$. The band gaps of $Ca_2Nb_2O_7$, $Ca_2Nb_{1.6}Ta_{0.4}O_7$, $Ca_2Nb_{1.2}Ta_{0.8}O_7$, $Ca_2Nb_{0.8}Ta_{1.2}O_7$, $Ca_2Nb_{0.4}Ta_{1.6}O_7$, and $Ca_2Ta_2O_7$ were estimated to be about 2.95, 3.05, 3.13, 3.42, 3.47, and 3.58 eV, respectively. For the $Ca_2Nb_{2-x}Ta_xO_7$ samples, the valence band potentials should be the same due to the same crystal structure. The difference of band gaps in the photocatalysts might result from that of the conduction band. Ta^{5+} substitution should increase the conduction band level of $Ca_2Nb_2O_7$. It is noteworthy that the onset of the diffuse reflection spectra with Ta substitution is not linearly shifted. The overall band gap of a given $Ca_2Nb_{2-x}Ta_xO_7$ compound can be thought to depend mainly upon two factors: (i) the degree of Ta 5d and Nb 4d orbitals being involved in the conduction band and (ii) the degree of delocalization of the excitation energy due to the distortion of the crystal structure arising from Ta substitution. It may thus be said that the change in the band gap energy is not necessarily proportional to that in the amount of Ta substitution; a similar result was also reported in a $Sr_2Nb_{2-x}Ta_xO_7$ solid solution.[6]

3.3. Effect of Ta^{5+} Substitution on Electronic Structures. The quantum-mechanical calculations performed here are based on density functional theory (DFT).[20] Exchange-correlation effects were taken into account by using the generalized gradient approximation (GGA).[21] The total energy code CASTEP was used,[22,23] which utilizes pseudo-potentials to describe electron−ion interactions and represents electronic wavefunctions using a plane-wave basis set. The kinetic energy cutoff was set at 380 eV. The Brillouin-zone sampling was performed by using a *k*-grid of 2 × 2 × 2 points for the calculations.

The calculated electronic band structures of $Ca_2Nb_2O_7$ and $Ca_2Ta_2O_7$ are shown in Figure 7. For the $Ca_2Nb_2O_7$ sample, the valence band was from −6.5 to 0 eV, and the conduction band was from 0.7 to 2.5 eV. The valence band of $Ca_2Ta_2O_7$ was from −6.5 to 0 eV, while the conduction band was from 1.6 to 4.1 eV. In addition, it is clear from this band structure that for both $Ca_2Nb_2O_7$ and $Ca_2Ta_2O_7$, the band gap appears between the highest point of the valence band and the lowest point of the conduction band at the same G point. Therefore, a direct optical transition can occur with no significant change in the wave vector for this compound. This direct band gap is one of the desirable properties of photocatalyst materials because light absorption for this kind of material can occur more efficiently as compared to that for materials with an indirect band gap. It is noteworthy that a larger curvature is observed in the conduction band of $Ca_2Ta_2O_7$ than that of $Ca_2Nb_2O_7$. As a consequence, the width of the conduction of $Ca_2Nb_2O_7$ is 1.6

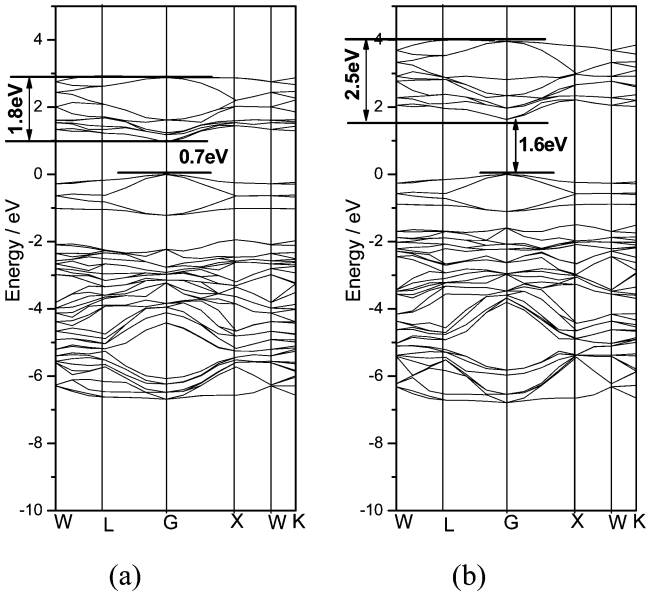

Figure 7. Electronic band structures of $Ca_2Nb_2O_7$ and $Ca_2Ta_2O_7$: (a) $Ca_2Nb_2O_7$ and (b) $Ca_2Ta_2O_7$.

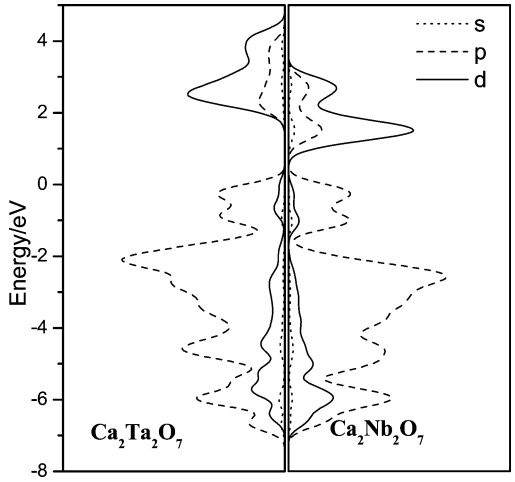

Figure 8. Projected partial density of states for $Ca_2Nb_2O_7$ and $Ca_2Ta_2O_7$.

eV, which is narrower than that of $Ca_2Ta_2O_7$ (2.5 eV). The mobility of the electronic carrier is proportional to the reciprocal effective mass of carrier that is in proportion to the curvature.[24] This means that $Ca_2Ta_2O_7$ has a larger electron mobility than $Ca_2Nb_2O_7$. This was also proven in the later photocurrent generation experiment.

Figure 8 shows the projected partial density of states for $Ca_2Nb_2O_7$ and $Ca_2Ta_2O_7$. The band gap energies of $Ca_2Nb_2O_7$ and $Ca_2Ta_2O_7$ are 0.7 and 1.6 eV, respectively, which are overly underestimated values as compared to the experimental band gap energies of 2.95 and 3.58 eV. The conduction band consists of mainly the d orbital of the transition metal (Nb or Ta) and a little O 2p, whereas the valence band consists of mainly O 2p and a little d orbital from the transition metal. The Ta^{5+} 5d band and the Nb^{5+} 4d band are both split into two main peaks: the lower part is a t_{2g} state, and the higher part is an e_g state. In addition, the states of Ta^{5+} 5d and Nb^{5+} 4d both heavily overlap with the O 2p states, which means that there is strong hybridization with the O 2p states. In the NbO_6 and TaO_6 octahedra, the O−M−O bond is mainly covalent.

Figure 9 shows the density contour maps for various bands of $Ca_2Nb_2O_7$. The electron density contour map for the band in the middle energy range of valence bands in $Ca_2Nb_2O_7$ is shown in Figure 9a. Both Nb 4d and O 2p orbitals are involved. Figure 9b is the contour map for the top of the valence band (HOMO). The electron density is localized to the O 2p orbitals only. The same result can be concluded in the case of $Ca_2Ta_2O_7$, which is not shown. Thus, these results indicate that in the valence band of $Ca_2Nb_2O_7$ and $Ca_2Ta_2O_7$, the lower part consists of the d (Nb 4d or Ta 5d) and O 2p orbitals, whereas the upper part is composed of O 2p orbitals. The electron density contour maps for the bottom of the conduction band (LUMO) and the band in the middle energy range of the conduction band of $Ca_2Nb_2O_7$ are shown in Figure 9c,d. The bottom of the conduction band is formed by Nb 4d orbitals, whereas the higher part consists of Nb 4d and O 2p orbitals. In the case of $Ca_2Ta_2O_7$, the LUMO is composed of Ta 5d, and the higher part is composed of Ta 5d and O 2p.

With the purpose of understanding as to how Ta substitution influences the electronic structures of $Ca_2Nb_2O_7$, theoretical calculations were also performed on $Ca_2Nb_{2-x}Ta_xO_7$ ($x = 0.5$ and 1.0). The calculated electronic band structures and density of states of $Ca_2Nb_{2-x}Ta_xO_7$ ($x = 0.5$ and 1.0) are shown in the Supporting Information. Figure 10 shows the conduction bands of $Ca_2Nb_{2-x}Ta_xO_7$ ($x = 0.5$ and 1.0); it was found that as more Nb is substituted with Ta, the conduction band becomes higher and has a larger curvature. The conduction bandwidth of $Ca_2Nb_{2-x}Ta_xO_7$ ($x = 0.5$) was about 2.2 eV, while that of $Ca_2Nb_{2-x}Ta_xO_7$ ($x = 1.0$) was 2.4 eV.

3.4. Effect of Ta^{5+} Substitution on Photocatalytic Activities. The photoactivities of the $Ca_2Nb_{2-x}Ta_xO_7$ samples were evaluated by degradation of FAD, a hazardous air pollutant as well as a common model compound to test the photodegradation capability of photocatalysts. Figure 11 shows time profiles of $\ln C/C_0$ under UV light irradiation ($\lambda = 254$ nm), where C is the concentration of FAD at irradiation time t, and C_0 is the concentration in the adsorption equilibrium on $Ca_2Nb_{2-x}Ta_xO_7$ before irradiation. The first-order linear relationship was revealed by the plots of $\ln C/C_0$ versus irradiation time. It is clearly seen that the photocatalytic activity of $Ca_2Ta_2O_7$ is better than that of $Ca_2Nb_2O_7$ under the same conditions. In the present work (except for CO_2, evolution from the reaction $HCHO + O_2 \rightarrow CO_2 + H_2O$), no intermediate reaction products were detected, which indicates that FAD decomposed to CO_2. The reaction rate constants (k) for the photodecomposition of FAD are given in the inset of Figure 11. When $x = 2$, $Ca_2Ta_2O_7$ showed the highest activity among $Ca_2Nb_{2-x}Ta_xO_7$ photocatalysts. With the increase of x, namely, with Ta substitution of Nb, the activity decreased first. However, when the value of x was larger than 1.2, the photocatalytic activity began to increase. $Ca_2Nb_{1.2}Ta_{0.8}O_7$ showed the lowest activity.

The photodegradation of RhB was also tested as a model reaction to evaluate the photocatalytic activity of the samples. The results are shown in Figure 12. As compared to the gaseous decomposition of FAD, the samples presented the same trend for the photodegradation of RhB. $Ca_2Ta_2O_7$ showed the highest activity among $Ca_2Nb_{2-x}Ta_xO_7$ photocatalysts and was approximately 2 times higher than that of $Ca_2Nb_2O_7$. In the region of $0 \le x \le 0.8$, the photocatalytic activity slightly decreased with Ta^{5+} substitution, while the activity increased with a value of x larger than 0.8.

For a comparison, we prepared $Ca_2Ta_2O_7$ by a conventional method using a solid-state reaction (SSR-$Ca_2Ta_2O_7$).[11] It was found that $Ca_2Ta_2O_7$ prepared by our method was 2 times faster than SSR-$Ca_2Ta_2O_7$ for the decomposition of FAD. In the photodegradation of RhB, $Ca_2Ta_2O_7$ prepared by our method

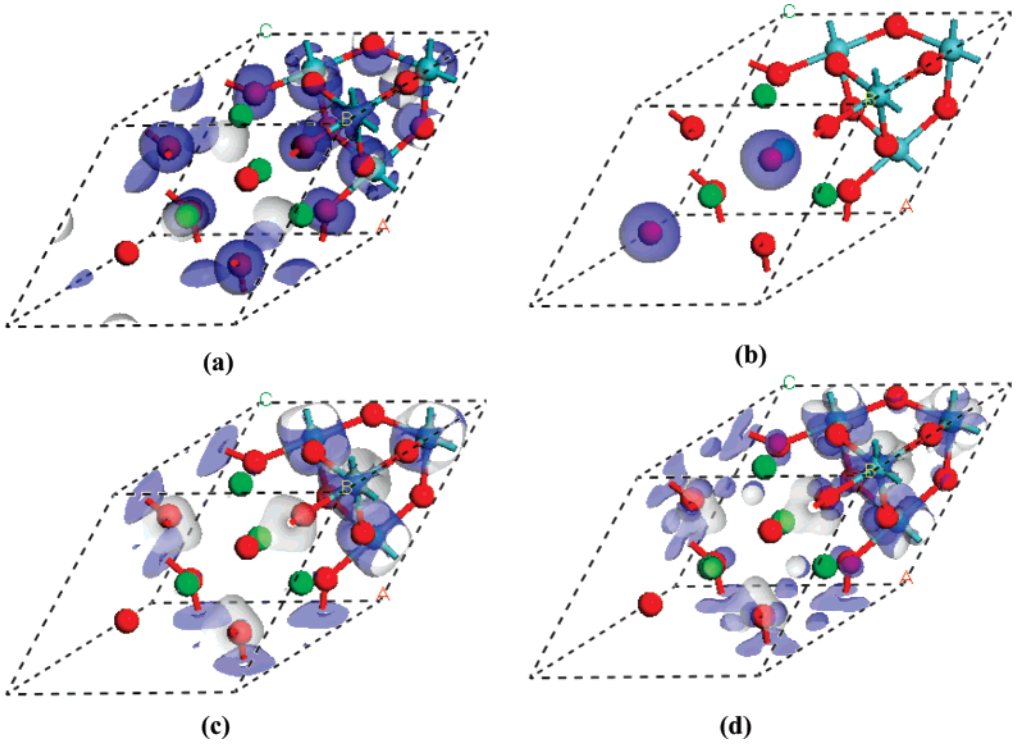

Figure 9. Electron density contour map for bands of $Ca_2Nb_2O_7$. (a) Band in the middle energy of the valence band. (b) Top of valence band (HOMO). (c) Bottom of conduction band. (d) Band in the middle energy of the conduction band.

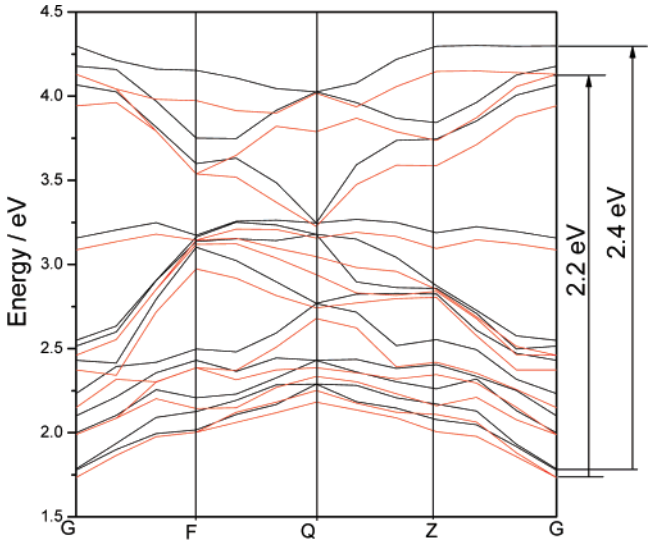

Figure 10. Conduction band structure of $Ca_2Nb_{2-x}Ta_xO_7$ ($x = 0.5$) (red lines) and conduction band structure of $Ca_2Nb_{2-x}Ta_xO_7$ ($x = 1.0$) (black lines).

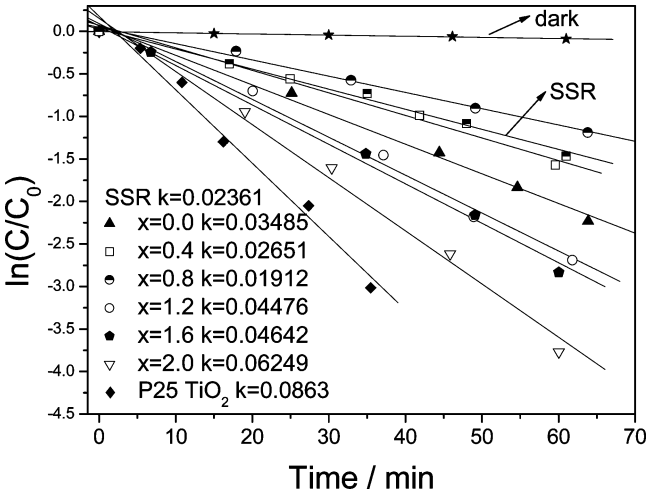

Figure 11. Catalytic activity for photodecomposition of FAD under UV light irradiation over $Ca_2Nb_{2-x}Ta_xO_7$.

was more than 5 times faster than that of SSR-$Ca_2Ta_2O_7$. This may be attributed to the large particle size of SSR-$Ca_2Ta_2O_7$, which results in a poor dispersion of catalyst in the solution. The hydrothermal sample has a priority to exert its photochemical activity due to its large surface area. Generally, e^-/h^+ recombination in the materials is divided into two categories: the volume recombination and the surface recombination. The volume recombination is a dominant process in well-crystallized bulk materials and is reduced by increasing the surface area of large particles. A larger surface area increases the available surface active sites and can lead to a higher photonic efficiency. The BET specific surface area of the hydrothermal sample was improved by about 60 times as compared to the sintered sample.[25] The surface e^-/h^+ recombination is mainly due to the abundant surface trapping sites and an insufficient driving force for e^-/h^+ pair separation.[26] Thus, the highly photocatalytic efficiency of the nanosized $Ca_2Ta_2O_7$ catalyst is expected by accelerating the interfacial charge carrier transfer processes, increasing the amount of the adsorbed organic compounds. Apart from the enhanced surface area, nanosized $Ca_2Ta_2O_7$ is expected to have a stronger oxidizing potential due to the nanosize effect. This could be an important reason as to why the hydrothermal sample exhibited enhanced photoactivity.

The photodecomposition of FAD and RhB in the presence of P-25 was also performed. The reaction rate constant (k) for the photodecomposition of FAD in the presence of P-25 was 0.0863, and nanosized $Ca_2Ta_2O_7$ exhibited a comparatively high photocatalytic activity ($k = 0.0625$). The catalyst showed a higher photoactivity for the decomposition of gaseous FAD than RhB in aqueous media. This could be due to the high density of 12.7 g cm^{-3} for $Ca_2Ta_2O_7$, and as a consequence, during the

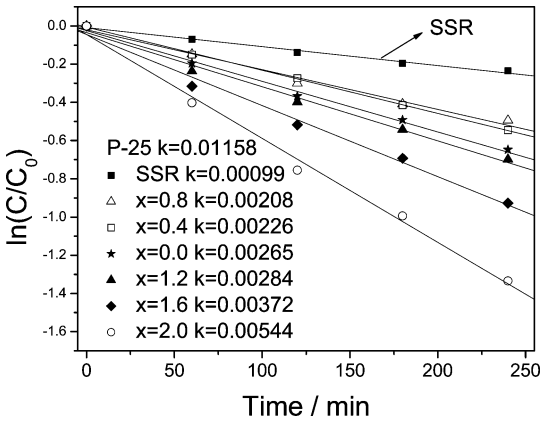

Figure 12. Catalytic activity for photodecomposition of RhB under UV light irradiation over $Ca_2Nb_{2-x}Ta_xO_7$.

course of the photochemical reaction, $Ca_2Ta_2O_7$ was accumulated at the bottom of the reaction vessel. However, in the case of P-25, the catalyst powder was suspended equally in the solution for a long time even after the experiment was finished. Undoubtedly, this shortcoming greatly limits the activity of the $Ca_2Ta_2O_7$ photocatalyst. Ways to further improve the dispersion of the catalyst are now under investigation and are expected to increase significantly the photocatalytic activity significantly.

3.5. Relationship of Conduction Band Structure and Photocatalytic Activity. In this work, all $Ca_2Nb_{2-x}Ta_xO_7$ samples were observed to share a similar phase structure and morphology if the same preparation process was used. We thought that the crystal sizes of the solid solutions might influence the photocatalytic activity to a small degree because Ta substitution did not significantly change the crystal sizes. The BET specific surface areas of $Ca_2Nb_2O_7$, $Ca_2Nb_{1.6}Ta_{0.4}O_7$, $Ca_2Nb_{1.2}Ta_{0.8}O_7$, $Ca_2Nb_{0.8}Ta_{1.2}O_7$, $Ca_2Nb_{0.4}Ta_{1.6}O_7$, and $Ca_2Ta_2O_7$ were measured to be about 39.9, 38.0, 38.1, 32.4, 31.4, and 28.5 $m^2\ g^{-1}$, respectively. The substitution of Ta decreased the surface areas of the photocatalysts; however, the photocatalytic activity of the solid solutions did not decrease with the surface area. In this work, the slight modifications of the crystal structure and electronic structure were considered to be the main factors influencing the photocatalytic activity in the present system. There are mainly two pathways in which Ta substitution can influence the electronic structure. First, the band gap varies as the composition changes. In the Ta substituted $Ca_2Nb_2O_7$ sample, as the Ta content increased, the band gap energies increased. The difference in the band gaps of $Ca_2Nb_{2-x}Ta_xO_7$ can be attributed to the composition of the conduction band; the conduction band of $Ca_2Nb_2O_7$ is composed of Nb 4d, while that of $Ca_2Nb_2O_7$ is Ta 5d. On the other hand, as the composition changes, the conduction band structure varies. Band structure calculations performed on Ta substituted $Ca_2Nb_2O_7$ found that the curvature of the conduction band became larger. The pentavalent ions Ta^{5+} and Nb^{5+} are often thought of as almost interchangeable because they have nearly identical ionic radii and oftentimes a very similar crystal chemistry. However, the effective electronegativity of 4d transition metal ions is higher than their 5d counterparts, and as a consequence, they should be expected to form more covalent bonds with oxygen, which would result in the formation of a narrower conduction band with a smaller curvature and possible delocalization of the charge carriers. A relatively narrow conduction band with a smaller curvature is not so effective for the movement of photogenerated electron−hole pairs,[27,28] and so the photocatalytic efficiencies decreased as the Ta^{5+} content decreased.

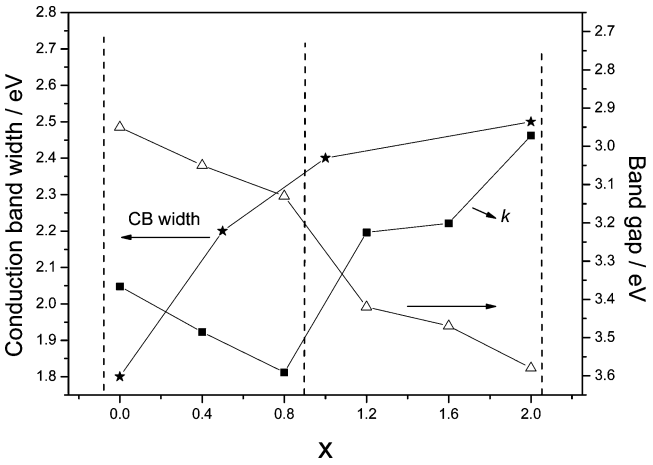

Figure 13. Curves of reaction rate constants *k*, band gap energies, and conduction bandwidth vs *x* in $Ca_2Nb_{2-x}Ta_xO_7$.

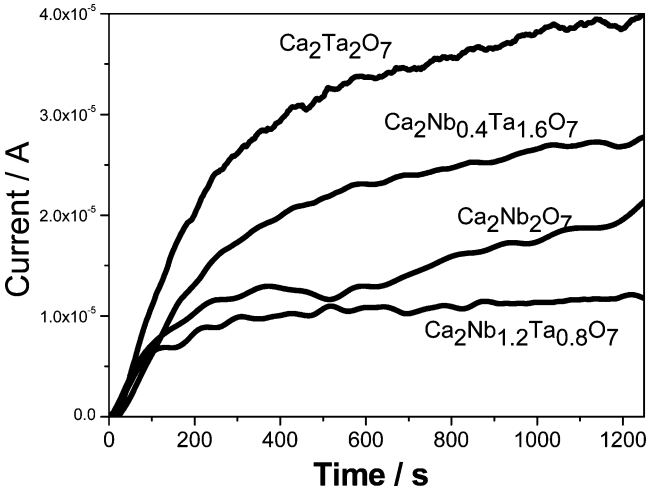

Figure 14. Photocurrent generated with time under UV irradiation suspended with acetate and Fe^{3+}.

The photoelectron transfer ability in semiconductor photocatalysts can be directly demonstrated by monitoring the photocurrent generation.[29] Figure 14 shows the photocurrents generated in photocatalyst suspensions under UV light. The photocurrent values order is consistent with the order of the photocatalytic activities. It can be seen that the $Ca_2Ta_2O_7$ sample generates the highest photocurrent among the samples, which is approximately 3 times faster than the sample of $Ca_2Nb_2O_7$. The superiority of $Ca_2Ta_2O_7$ over $Ca_2Nb_2O_7$ as expected from the more dispersed conduction band is confirmed. The $Ca_2Nb_{1.2}Ta_{0.8}O_7$ sample exhibited the lowest photocurrent, and although the width of the conduction band is larger than that of $Ca_2Nb_2O_7$, the reason will be discussed in the future.

The photoelectron transfer is improved by Ta^{5+} substitution due to the formation of a conduction band with a large curvature; thus, the photocatalytic activity should increase as there is more Ta^{5+} substitution. However, $Ca_2Nb_{1.2}Ta_{0.8}O_7$ and $Ca_2Nb_{1.6}Ta_{0.4}O_7$ showed lower activities than that of $Ca_2Nb_2O_7$, even if they had a relatively wide conduction band due to Ta substitution. These observations indicated that the photocatalytic activities depended upon not only the conduction bandwidth but also upon other factors. One of the reasons for the decrease in the activity is that the number of available photons decreased with the extension of a band gap. Figure 13 shows the curves of reaction rate constants (*k*), band gap energies, and conduction bandwidths versus *x* in $Ca_2Nb_{2-x}Ta_xO_7$. As the ratio of tantalum and niobium in $Ca_2Nb_{2-x}Ta_xO_7$ is increased, the amount of

absorbed photons would become smaller because of the increase of the band gap energy. Another possible reason might be related to the lattice defects. Lattice defects may act as recombination centers for photoinduced electrons and holes, thus reducing the photocatalytic activity significantly.[30,31] A lattice distortion might exist around the tantalum substitution.[32] Such a lattice distortion could act as a recombination center, leading to a drop in the photocatalytic activity.

4. Conclusion

Ultra-fine $Ca_2Nb_{2-x}Ta_xO_7$ ($0 \leq x \leq 2$) photocatalysts were synthesized by a hydrothermal method at a low temperature. The photocatalytic activity and photocurrent generation were effectively improved by Ta^{5+} substitution. The improvement of photoactivity can be explained as $Ca_2Ta_2O_7$ preferred to form a larger curvature of the conduction band than $Ca_2Nb_2O_7$ due to the electronegativity difference of Nb 4d and Ta 5d.

Acknowledgment. This work was partly supported by the Chinese National Science Foundation (20433010 and 20571047 and National Basic Research Program of China (2007CB613303).

Supporting Information Available: Structure models for $Ca_2Nb_{1.5}Ta_{0.5}O_7$ and Ca_2NbTaO_7. Band dispersion and density of states for optimized structure of $Ca_2Nb_{1.5}Ta_{0.5}O_7$ and Ca_2NbTaO_7. PDOS for Ca, Nb, Ta, and O of $Ca_2Nb_2O_7$ and $Ca_2Ta_2O_7$. This information is available free of charge via the Internet at http://pubs.acs.org.

References and Notes

(1) Subramanian, M. A.; Aravamudan, G.; Subba Rao, G. V. *Prog. Solid State Chem.* **1983**, *15*, 55. Ashbrook, S. E.; Whittle, K. R.; Lumpkin, G. R.; Farnan, I. *J. Phys. Chem. B* **2006**, *110*, 10358.

(2) Abe, R.; Higashi, M.; Sayama, K.; Abe, Y.; Sugihara, H. *J. Phys. Chem. B* **2006**, *110*, 2219.

(3) Zou, Z.; Ye, J.; Abe, R.; Arakawa, H. *Catal. Lett.* **2000**, *68*, 235.

(4) Zou, Z.; Ye, J.; Sayama, K.; Arakawa, H. *Chem. Phys. Lett.* **2001**, *343*, 303.

(5) Zou, Z.; Ye, J.; Arakawa, H. *Solid State Commun.* **2002**, *119*, 471.

(6) Yoshino, M.; Kakihana, M.; Cho, W. S.; Kato, H.; Kudo, A. *Chem. Mater.* **2002**, *14*, 3369.

(7) Zou, Z.; Ye, J.; Arakawa, H. *Chem. Mater.* **2001**, *13*, 1765.

(8) Tang, J.; Zou, Z.; Ye, J. *Chem. Mater.* **2004**, *16*, 1644.

(9) Cava, R. J.; Krajewski, J. J.; Roth, R. S. *Mater. Res. Bull.* **1998**, *33*, 527.

(10) Fiedziuszko, S. J.; Hunter, I. C.; Itoh, T. *IEEE Trans. Microwave Theory* **2002**, *50*, 706.

(11) Brandon, J. K.; Megaw, H. D. *Philos. Mag.* **1970**, *21*, 189. Carpy, A.; Amestov, P.; Galy, J. *C. R. Acad. Sci. Paris* **1972**, *833*, 275.

(12) Aleshin, E.; Roy, R. *J. Am. Ceram. Soc.* **1962**, *18*, 45.

(13) Lamure, J.; Colas, J. L. *C. R. Acad. Sci. Paris* **1970**, *270*, 700.

(14) Lewandowski, J. T.; Pickering, I. J. *Mater. Res. Bull.* **1992**, *27*, 981.

(15) Yamagushi, O.; Tomihisa, D.; Shirai, M.; Shimizu, K. *J. Am. Ceram. Soc.* **1988**, *71*, 260.

(16) Zafrir, M.; Aladjem, A.; Zilber, R. *J. Solid State Chem.* **1976**, *18*, 377.

(17) Shannon, R. D. *Acta Crystallogr., Sect. A: Found. Crystallogr.* **1976**, *32*, 751.

(18) Surendran, K. P.; Sebastian, M. T.; Mohanan, P.; Moreira, R. L.; Dias, A. *Chem. Mater.* **2005**, *17*, 142.

(19) Chen, Y.; Fierro, J. L. G.; Tanaka, T.; Wachs, I. E. *J. Phys. Chem. B* **2003**, *107*, 5243.

(20) Kohn, W.; Sham, L. J. *Phys. Rev. A: At., Mol., Opt. Phys.* **1965**, *140*, 1133.

(21) Perdew, J. P.; Wang, Y. *Phys. Rev. B: Condens. Matter Mater. Phys.* **1992**, *45*, 13244.

(22) Payne, M. C.; Teter, M. P.; Allan, D. C.; Arias, T. A.; Joannopoulos, J. D. *Rev. Mod. Phys.* **1992**, *64*, 1045.

(23) CASTEP program was developed and distributed by Molecular Simulations Inc., San Diego, CA.

(24) Matsushima, S.; Nakamura, H.; Arai, M.; Xu, C. *Chem. Lett.* **2002**, 700.

(25) Tang, J.; Zou, Z.; Ye, J. *Catal. Lett.* **2004**, *92*, 53.

(26) Yasuo, E.; Takayoshi, S.; Masaru, H.; Mamoru, W. *Chem. Mater.* **2002**, *14*, 4309.

(27) Xu, J.; Greenblatt, M. *J. Solid State Chem.* **1996**, *121*, 273.

(28) Xu, J.; Ramanujachary, K. V.; Hohn, P.; Greenblatt, M. *J. Solid State Chem.* **1996**, *125*, 192.

(29) Park, H.; Choi, W. *J. Phys. Chem. B* **2003**, *107*, 3885. Kim, H. G.; Borse, P. H.; Choi, W. J.; Lee, S. *Angew. Chem., Int. Ed.* **2005**, *44*, 4585.

(30) Yoshino, M.; Kakihana, M.; Cho, W.; Kato, H.; Kudo, A. *Chem. Mater.* **2002**, *14*, 3369.

(31) Yu, J.; Ho, W.; Yu, J.; Yip, H.; Wong, P.; Zhao, J. *Environ. Sci. Technol.* **2005**, *39*, 1175.

(32) Kato, H.; Kudo, A. *J. Photochem. Photobiol., A* **2001**, *145*, 129.

(33) Yin, J.; Zou, Z.; Ye, J. *J. Mater. Res.: Rapid Commun.* **2002**, *17*, 9.

(34) Butler, M. A. *J. Appl. Phys.* **1977**, *48*, 1914.